arXiv:1601.04977v1 [cond-mat.str-el] 19 Jan 2016

Ab Initio Quantum Monte Carlo Simulations of the Uniform Electron Gas without Fixed Nodes II: Unpolarized Case

T. Dornheim[1,†], S. Groth[1,†], T. Schoof[1], C. Hann[1,2], and M. Bonitz[1*]
[†] *These authors contributed equally to this work.*
[1] *Institut für Theoretische Physik und Astrophysik, Christian-Albrechts-Universität zu Kiel, D-24098 Kiel, Germany*
[2] *Department of Physics, Duke University, Durham, North Carolina 27708, USA*
(Dated: January 20, 2016)

In a recent publication [S. Groth *et al.*, PRB (2016)], we have shown that the combination of two novel complementary quantum Monte Carlo approaches, namely configuration path integral Monte Carlo (CPIMC) [T. Schoof *et al.*, PRL **115**, 130402 (2015)] and permutation blocking path integral Monte Carlo (PB-PIMC) [T. Dornheim *et al.*, NJP **17**, 073017 (2015)], allows for the accurate computation of thermodynamic properties of the spin-polarized uniform electron gas (UEG) over a wide range of temperatures and densities without the fixed-node approximation. In the present work, we extend this concept to the unpolarized case, which requires non-trivial enhancements that we describe in detail. We compare our new simulation results with recent restricted path integral Monte Carlo data [E. Brown *et al.*, PRL **110**, 146405 (2013)] for different energy contributions and pair distribution functions and find, for the exchange correlation energy, overall better agreement than for the spin-polarized case, while the separate kinetic and potential contributions substantially deviate.

PACS numbers: 05.30-d, 05.30.Fk, 71.10.Ca, 02.70.Ss

I. INTRODUCTION

Quantum Monte Carlo (QMC) simulations of fermions are of paramount importantance to describe manifold aspects of nature. In particular, recent experimental progress with highly compressed matter [1–3] such as plasmas in laser fusion experiments [4–9] and solids after laser irradiation [10], but also the need for an appropriate description of compact stars and planet cores [11–13], has lead to a high demand for accurate simulations of electrons in the warm dense matter (WDM) regime. Unfortunately, the application of all QMC methods to fermions is severely hampered by the fermion sign problem (FSP) [14, 15]. A popular approach to circumvent this issue is the restricted path integral Monte Carlo (RPIMC) [16] method, which, however, is afflicted with an uncontrollable error due the fixed node approximation[17–20]. Therefore, until recently, the quality of the only available QMC results for the uniform electron gas (UEG) in the WDM regime [21] has remained unclear.

To address this issue, in a recent publication (paper I, Ref. [22]) we have combined two novel complementary approaches: our configuration path integral Monte Carlo (CPIMC) method [23–25] excels at high to medium density and arbitrary temperature, while our permutation blocking path integral Monte Carlo (PB-PIMC) approach [26, 27] significantly extends standard fermionic PIMC [28, 29] towards lower temperature and higher density. Surprisingly, it has been found that existing RPIMC results are inaccurate even at high temperatures.

However, although the spin-polarized systems that have been investigated in our previous works are of relevance for the description of e.g. ferromagnetic materials or strongly magnetized systems, they constitute a rather special case, since most naturally occuring plasmas are predominantly unpolarized. Therefore, in the present work we modify both our implementations of PB-PIMC and CPIMC to simulate the unpolarized UEG. So far only a single data set for a small system ($N = 14$ electrons, one isotherm) could be obtained in our previous work [25] because the paramagnetic case turns out to be substantially more difficult than the ferromagnetic one. Therefore, we have developed novel nontrivial enhancements of our CPIMC algorithm that are discussed in detail. With these improvements, we are able to present accurate results for different energies for the commonly used case of $N = 66$ unpolarized electrons over a broad range of parameters.

Since many details of our approach have been presented in our paper I [22], in the remainder of this paper we restrict ourselves to a brief, but selfcontained introduction to CPIMC and PB-PIMC and focus on the differences arising from their application to the unpolarized UEG, compared to the polarized case. In section II, we introduce the model Hamiltonian, both in coordinate space (II A) and second quantization (II B) and, subsequently, provide a brief introduction to the employed QMC approaches (Sec. III), namely PB-PIMC (III A) and CPIMC (III B). Finally, in Sec. IV, we present combined results from both methods for the exchange correlation, kinetic, and potential energy (IV A) as well as the pair distribution function (IV B). Further, we compare our data to those from RPIMC [21], where available. While we find better agreement than for the spin-polarized case [22, 27], there nevertheless appear significant deviations towards lower temperature.

*Electronic address: bonitz@physik.uni-kiel.de

II. HAMILTONIAN OF THE UNIFORM ELECTRON GAS

The uniform electron gas ("Jellium") is a model system of Coulomb interacting electrons in a neutralizing homogeneous background. As such, it explicitly allows one to study effects due to the correlation and exchange of the electrons, whereas those due to the positive ions are neglected. Furthermore, the widespread density functional theory (DFT) crucially depends on ab initio results for the exchange correlation energy of the uniform electron gas (UEG), hitherto at zero temperature [30]. However, it is widely agreed that the appropriate treatment of matter under extreme conditions requires to go beyond ground state DFT, which, in turn, needs accurate results for the finite temperature UEG. While the electron gas itself is defined as an infinite macroscopic system, QMC simulations are possible only for a finite number of particles N. Hence, we always assume periodic boundary conditions and include the interaction of the N electrons in the main simulation cell with all their images via Ewald summation and defer any additional finite-size corrections [31–33] to a future publication.

A. Coordinate representation of the Hamiltonian

Following Refs. [27, 31], we express the Hamiltonian (we measure energies in Rydberg and distances in units of the Bohr radius a_0) for $N = N_\uparrow + N_\downarrow$ unpolarized electrons in coordinate space as

$$\hat{H} = -\sum_{i=1}^{N} \nabla_i^2 + \sum_{i=1}^{N}\sum_{j\neq i}^{N} e^2\Psi(\mathbf{r}_i,\mathbf{r}_j) + Ne^2\xi \,, \tag{1}$$

with the well-known Madelung constant ξ and the periodic Ewald pair interaction

$$\begin{aligned}\Psi(\mathbf{r},\mathbf{s}) &= \frac{1}{V}\sum_{\mathbf{G}\neq 0}\frac{e^{-\pi^2\mathbf{G}^2/\kappa^2}e^{2\pi i\mathbf{G}(\mathbf{r}-\mathbf{s})}}{\pi\mathbf{G}^2} \\ &- \frac{\pi}{\kappa^2 V} + \sum_{\mathbf{R}}\frac{\mathrm{erfc}(\kappa|\mathbf{r}-\mathbf{s}+\mathbf{R}|)}{|\mathbf{r}-\mathbf{s}+\mathbf{R}|} \,. \end{aligned}\tag{2}$$

Here $\mathbf{R} = \mathbf{n}_1 L$ and $\mathbf{G} = \mathbf{n}_2/L$ denote the real and reciprocal space lattice vectors, respectively, with the box length L, volume $V = L^3$ and the usual Ewald parameter κ. Furthermore, PB-PIMC simulations require the evaluation of all forces within the system, where the force between two electrons i and j is given by

$$\begin{aligned}\mathbf{F}_{ij} &= \frac{2}{V}\sum_{\mathbf{G}\neq 0}\left(\frac{\mathbf{G}}{\mathbf{G}^2}\sin\left[2\pi\mathbf{G}(\mathbf{r}_i-\mathbf{r}_j)\right]e^{-\pi^2\mathbf{G}^2/\kappa^2}\right) \\ &+ \sum_{\mathbf{R}}\frac{\mathbf{r}_i-\mathbf{r}_j+\mathbf{R}}{\alpha^3}\left(\mathrm{erfc}(\kappa\alpha)+\frac{2\kappa\alpha}{\sqrt{\pi}}e^{-\kappa^2\alpha^2}\right) \,, \end{aligned}\tag{3}$$

with the definition $\alpha = |\mathbf{r}_i - \mathbf{r}_j + \mathbf{R}|$.

B. Hamiltonian in second quantization

In second quantization with respect to spin-orbitals of plane waves, $\langle \mathbf{r}\sigma\,|\mathbf{k}_i\sigma_i\rangle = \frac{1}{L^{3/2}}e^{i\mathbf{k}_i\cdot\mathbf{r}}\delta_{\sigma,\sigma_i}$ with $\mathbf{k}_i = \frac{2\pi}{L}\mathbf{m}_i$, $\mathbf{m}_i \in \mathbb{Z}^3$ and $\sigma_i \in \{\uparrow,\downarrow\}$, the model Hamiltonian, Eq. (1), takes the form

$$\hat{H} = \sum_i \mathbf{k}_i^2 \hat{a}_i^\dagger \hat{a}_i + 2\sum_{\substack{i<j,k<l\\ i\neq k, j\neq l}} w^-_{ijkl}\hat{a}_i^\dagger\hat{a}_j^\dagger\hat{a}_l\hat{a}_k + Ne^2\xi, \tag{4}$$

with the antisymmetrized two-electron integrals, $w^-_{ijkl} = w_{ijkl} - w_{ijlk}$, where

$$w_{ijkl} = \frac{4\pi e^2}{L^3(\mathbf{k}_i-\mathbf{k}_k)^2}\delta_{\mathbf{k}_i+\mathbf{k}_j,\mathbf{k}_k+\mathbf{k}_l}\delta_{\sigma_i,\sigma_k}\delta_{\sigma_j,\sigma_l} \,, \tag{5}$$

and the Kronecker deltas ensuring both momentum and spin conservation. The first (second) term in the Hamiltonian Eq. (4) describes the kinetic (interaction) energy. The operator $\hat{a}_i^\dagger$ ($\hat{a}_i$) creates (annihilates) a particle in the spin-orbital $|\mathbf{k}_i\sigma_i\rangle$.

III. FERMIONIC QUANTUM MONTE CARLO WITHOUT FIXED NODES

Throughout the entire work, we consider the canonical ensemble, i.e., the volume V, particle number N and inverse temperature $\beta = 1/k_\mathrm{B}T$ are fixed. In equilibrium statistical mechanics, all thermodynamic quantities can be derived from the partition function

$$Z = \mathrm{Tr}\hat{\rho} \,, \tag{6}$$

which is of central importance for any QMC formulation and defined as the trace over the canonical density operator

$$\hat{\rho} = e^{-\beta\hat{H}} \,. \tag{7}$$

The expectation value of an arbitrary operator $\hat{A}$ is given by

$$\langle\hat{A}\rangle = \frac{\mathrm{Tr}(\hat{A}\hat{\rho})}{\mathrm{Tr}\hat{\rho}} = \frac{1}{Z}\mathrm{Tr}(\hat{A}\hat{\rho}) \,. \tag{8}$$

However, for an appropriate description of fermions, Eqs. (6) and (8) must be extended either by antisymmetrizing $\hat{\rho} \to \hat{\rho}^-$ or the trace itself [23], $\mathrm{Tr} \to \mathrm{Tr}^-$. Therefore, it holds

$$Z = \mathrm{Tr}\hat{\rho}^- = \mathrm{Tr}^-\hat{\rho} \,. \tag{9}$$

While defining the trace in Eq. (9) as either expression does not change the well-defined thermodynamic expectation values, it does lead to rather different formulations of the same problem. The combination of antisymmetrizing the density matrix and evaluating the trace in coordinate space is the first step towards both standard

PIMC and PB-PIMC, cf. Sec. III A, but also RPIMC. All these approaches share the fact that they are efficient when fermionic quantum exchange does not yet dominate a systm, but they will become increasingly costly towards low temperature and high density. Switching to second quantization and carrying out the trace in antisymmetrized Fock space, on the other hand, is the basic idea behind our CPIMC method, cf. Sec. III B, and, in a different way, behind the likewise novel density matrix QMC method [34]. The latter approach has recently been applied to the the case of $N = 4$ spin-polarized electrons [35], where complete agreement with our CPIMC results [24] was reported. These QMC approaches tend to excel at high density, i.e., weak nonideality, and become eventually unfeasible towards stronger coupling strength.

Therefore, it is a natural strategy to combine different representations at complementary parameter ranges as this does effectively allow to circumvent the numerical shortcomings with which every single fermionic QMC method is necessarily afflicted [22, 27].

A. Permutation blocking PIMC

1. *Basic idea*

In this section, we will briefly introduce our permutation blocking PIMC approach. A more detailed description of the method itself and its application to the spin-polarized UEG can be found in Refs. [26, 27].

The basic idea behind PB-PIMC is essentially equal to standard PIMC in coordinate space, e.g., Ref. [29], but, in addition, combines two well-known concepts: 1) antisymmetric imaginary time propagators, i.e., determinants [36–38], and 2) a fourth-order factorization of the density matrix [39–42]. Furthermore, since this leads to a significantly more complicated configuration space without any fixed paths, one of us has developed an efficient set of Metropolis Monte Carlo [43] updates that utilize the temporary construction of artificial trajectories [26]. As mentioned above, we evaluate the trace within the canonical partition function for $N = N_\uparrow + N_\downarrow$ unpolarized electrons in coordinate representation

$$\begin{aligned} Z &= \frac{1}{N_\uparrow! N_\downarrow!} \sum_{\sigma_\uparrow \in S_{N_\uparrow}} \sum_{\sigma_\downarrow \in S_{N_\downarrow}} \mathrm{sgn}(\sigma_\uparrow)\, \mathrm{sgn}(\sigma_\downarrow) \\ &\quad \times \int \mathrm{d}\mathbf{R}\ \langle \mathbf{R}|\, e^{-\beta \hat{H}}\, |\hat{\pi}_{\sigma_\uparrow} \hat{\pi}_{\sigma_\downarrow} \mathbf{R}\rangle\ , \end{aligned} \tag{10}$$

with $\hat{\pi}_{\sigma_{\uparrow,\downarrow}}$ being the exchange operator that corresponds to a particular element $\sigma_{\uparrow,\downarrow}$ from the permutation group $S_{N_{\uparrow,\downarrow}}$ with associated sign $\mathrm{sgn}(\sigma_{\uparrow,\downarrow})$ and $\uparrow$ ($\downarrow$) denoting spin-up (spin-down) electrons. However, since the kinetic and potential contributions to the Hamiltonian, $\hat{K}$ and $\hat{V}$, do not commute, the low-temperature matrix elements of $\hat{\rho}$ are not known. To overcome this issue, we use the common group property $\hat{\rho}(\beta) = \prod_{\alpha=0}^{P-1} \hat{\rho}(\epsilon)$ of the density matrix, with $\epsilon = \beta/P$, and approximate each of the P factors at a P times higher temperature by the fourth-order factorization [40, 41]

$$\begin{aligned} e^{-\epsilon \hat{H}} &\approx e^{-v_1 \epsilon \hat{W}_{a_1}} e^{-t_1 \epsilon \hat{K}} e^{-v_2 \epsilon \hat{W}_{1-2a_1}} \\ &\quad \times e^{-t_1 \epsilon \hat{K}} e^{-v_1 \epsilon \hat{W}_{a_1}} e^{-2t_0 \epsilon \hat{K}}\ . \end{aligned} \tag{11}$$

It should be noted that Eq. (11) allows for sufficient accuracy, even for small P. The $\hat{W}$ operators in Eq. (11) denote a modified potential that combines the usual potential energy $\hat{V}$ with double commutator terms of the form

$$[[\hat{V}, \hat{K}], \hat{V}] = \frac{\hbar^2}{m} \sum_{i=1}^{N} |\mathbf{F}_i|^2\ ,\ \mathbf{F}_i = -\nabla_i V(\mathbf{R})\ , \tag{12}$$

and, therefore, require the evaluation of all forces within the system, cf. Eq. (3). The final result for the PB-PIMC partition function is given by

$$\begin{aligned} Z &= \frac{1}{(N_\uparrow! N_\downarrow!)^{3P}} \int \mathrm{d}\mathbf{X} \\ &\quad \prod_{\alpha=0}^{P-1} \left(e^{-\epsilon \tilde{V}_\alpha} e^{-\epsilon^3 u_0 \frac{\hbar^2}{m} \tilde{F}_\alpha} D_{\alpha,\uparrow} D_{\alpha,\downarrow} \right)\ , \end{aligned} \tag{13}$$

with $\tilde{V}_\alpha$ and $\tilde{F}_\alpha$ containing all contributions of the potential energy and the forces, respectively. The exchange-diffusion functions are defined as

$$\begin{aligned} D_{\alpha,\uparrow} &= \det(\rho_{\alpha,\uparrow}) \det(\rho_{\alpha A,\uparrow}) \det(\rho_{\alpha B,\uparrow}) \\ D_{\alpha,\downarrow} &= \det(\rho_{\alpha,\downarrow}) \det(\rho_{\alpha A,\downarrow}) \det(\rho_{\alpha B,\downarrow}) \end{aligned} \tag{14}$$

and contain the determinants of the diffusion matrices

$$\rho_{\alpha,\uparrow}(i,j) = \lambda_{t_1\epsilon}^{-3} \sum_{\mathbf{n}} e^{-\frac{\pi}{\lambda_{t_1\epsilon}^2} (\mathbf{r}_{\alpha,\uparrow,j} - \mathbf{r}_{\alpha A,\uparrow,i} + \mathbf{n}L)^2}\ , \tag{15}$$

with $\lambda_{t_1\epsilon} = \sqrt{2\pi\epsilon t_1 \hbar^2/m}$ being the thermal wavelength of a single "time slice".

In contrast to standard PIMC, where each permutation cycle has to be explicitly sampled, we combine both positively and negatively signed configuration weights in the determinants both for the spin-up and spin-down electrons. This leads to a cancellation of many terms and, consequently, a significantly increased average sign in our Monte Carlo simulations. Yet, this "permutation blocking" is only effective when $\lambda_{t_1\epsilon}$ is comparable to the mean inter-particle distance, i.e., when there are both large diagonal and off-diagonal elements in the diffusion matrices. With an increasing number of high-temperature factors P, $\lambda_{t_1\epsilon}$ decreases and, eventually, when there is only but a single large element in each row of the $\rho_{\alpha,\uparrow}$, the average sign converges towards that of standard PIMC. For this reason, it is crucial to combine the determinants from the antisymmetric propagators with a higher order factorization of the density matrix, cf. Eq. (11). It is only this combination which allows for sufficient accuracy with

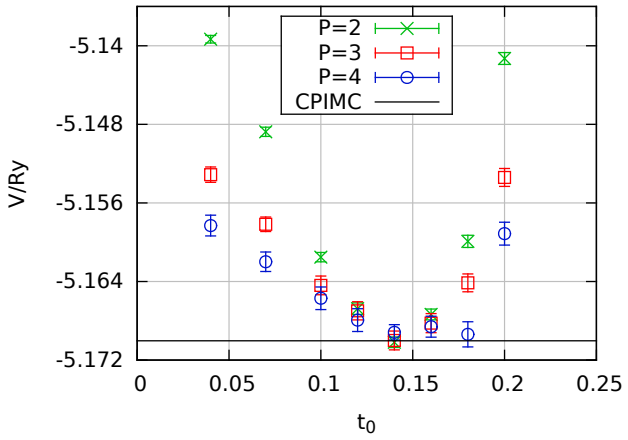

Figure 1: Influence of the relative interslice spacing t_0 on the convergence – The potential energy from PB-PIMC simulations of $N = 4$ unpolarized electrons at $\theta = 0.5$ and $r_s = 1$ is plotted versus t_0 for the fixed choice $a_1 = 0.33$.

as few as two or three propagators while, at the same time, the benefit of the blocking within the determinants is maximized. Furthermore, we note that electrons with different spin-projections do not exchange at all. Therefore, PB-PIMC simulations of the unpolarized UEG with $N = N_\uparrow + N_\downarrow$ do suffer from a significantly less severe sign problem than for $N = 2N_\uparrow$ spin-polarized electrons.

2. *Application to the unpolarized UEG*

The accuracy of our PB-PIMC simulations crucially depends on the systematic error due to the employed higher order factorization [26, 27]. Thus, we begin the investigation of the unpolarized electron gas with the analysis of the convergence behavior with respect to the two free parameters from Eq. (11), namely a_0 (weighting the contributions of the forces on different time slices) and t_0 (controlling the relative interslice spacing). In Fig. 1, we set $a_0 = 0.33$ fixed, which corresponds to equally weighted forces on all slices, and plot the potential energy for $P = 2, 3, 4$ over the entire t_0-range for a benchmark system of $N = 4$ unpolarized electrons at $r_s = 1$ and $\theta = 0.5$. Evidently, for all t_0 values V converges monotonically from above towards the exact result, which has been obtained with CPIMC. The optimum value for t_0 is located around $t_0 = 0.14$, where all three PB-PIMC values are within single error bars with the black line. For completeness, we mention that this particular set of the optimum free parameters for the energy is consistent with the previous findings for different systems [26, 27, 41].

A natural follow-up question is how the convergence with P behaves with respect to the density parameter r_s. In Fig. 2, we show results for the relative error of the potential ($\Delta V/|V|$, panel a) and kinetic energy ($\Delta K/K$, panel b), where the reference values are again obtained

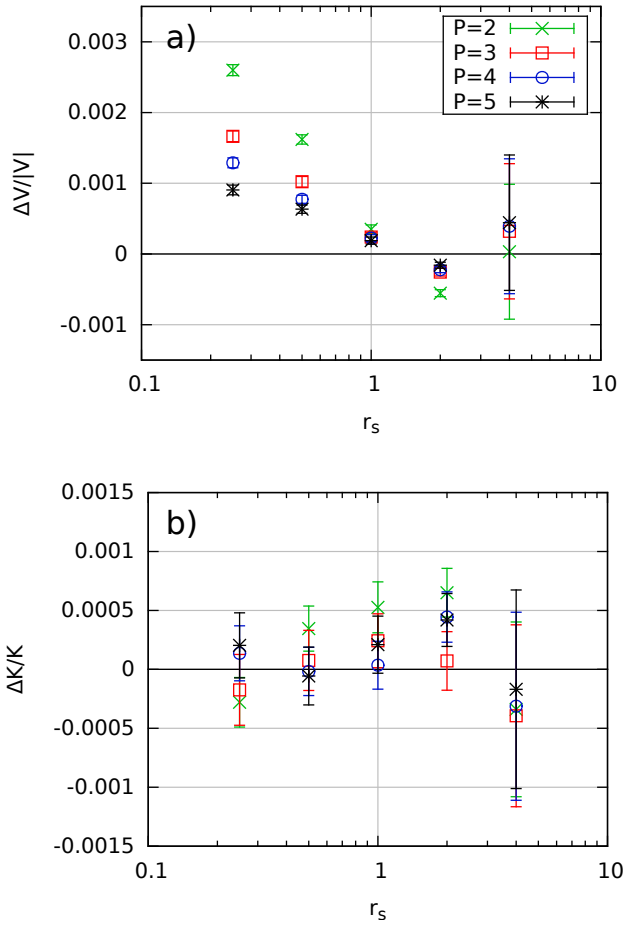

Figure 2: Density dependence of the relative time step error from PB-PIMC with $a_1 = 0.33$ and $t_0 = 0.14$ – The relative differences between PB-PIMC results with $P = 2, 3, 4, 5$ and reference data from CPIMC are plotted versus r_s for the potential energy (a) and the kinetic energy (b).

from CPIMC. The statistical uncertainty is mainly due to PB-PIMC, except for $r_s = 4$ where the CPIMC error bar predominates. For the kinetic energy, even for $P = 3$ there are no clear systematic deviations from the exact result over the entire r_s-range. Only with two propagators, our results for K appear to be slightly too large for $r_s \in (0.5, 1, 2)$, although this trend hardly exceeds $\Delta K/K = 5 \times 10^{-4}$. For the potential energy, the factorization error behaves quite differently. For $r_s \geq 1$, even with two propagators the accuracy is better than 0.1%, while towards higher density ($r_s < 1$), the convergence significantly deteriorates. In particular, at $r_s = 0.25$ even with $P = 5$ there is a deviation of $\Delta V/|V| \approx 0.1\%$. This observation is in striking contrast to our previous investigation of the polarized UEG, where the relative error in both K and V decreased towards $r_s \to 0$. The reason for this trend lies in the presence of two different particle species which do not exchange with each other, namely $N_\uparrow$ spin-up and $N_\downarrow$ spin-down electrons. Even at high

density, two electrons from the same species are effectively separated by their overlapping kinetic density matrices that cancel in the determinants, which is nothing else than the Pauli blocking. Yet, a spin-up and a spin-down electron do not experience such a repulsion and, at weak coupling (small r_s), can be separated by much smaller distances r from each other. With decreasing r the force terms in Eq. (11) that scale as $F(r) \propto 1/r^2$ will eventually exceed the Coulomb potential $V(r) \propto 1/r$, i.e., the higher order correction predominates. This trend must be compensated by an increasing number of propagators P. Hence, the fermionic nature of the electrons that manifests as the Pauli blocking significantly enhances the performance of our factorization scheme, which means that the simulation of unpolarized systems is increasingly hampered towards high density. In addition to the Monte Carlo inherent sign problem, this is a further reason to combine PB-PIMC with CPIMC, since the latter excels just in this regime.

In our recent analysis of PB-PIMC for electrons in a $2D$ harmonic trap [26], it was found that, while the combination $a_0 = 0.33$ and $t_0 = 0.14$ (parameter set a) is favorable for a fast convergence of the energy, it does not perform so well for other properties like, in that case, the density profile. To address this issue, we again simulate a benchmark system of $N = 4$ unpolarized electrons and compute the pair distribution function $g(r)$, see, e.g. Ref. [44] for a comprehensive discussion. In Fig. 3, we show results for the above combination of free parameters (a) and $P = 2, 3, 4, 5$. Panel a) displays the data for the inter-species distribution function $g_{\uparrow\downarrow}$. We note that, for the infinite UEG, this quantity approaches unity at large distances, but the small simulation box for $N = 4$ restricts us to the depicted r-range. All four curves deviate from each other for $r \lesssim 0.5$, which indicates that $g_{\uparrow\downarrow}$ is not yet converged even for $P = 5$ at small distances, and are equal otherwise. This is again a clear indication of the shortcomings of our fourth-order factorization, which overestimates the Coulomb repulsion at short ranges. The intra-species distribution function $g_{\uparrow\uparrow} = g_{\downarrow\downarrow}$, which is shown in panel b), does not exhibit such a clear trend since only the green curve that corresponds to $P = 2$ can be distinguished from the rest. This is, of course, expected and a consequence of the Pauli blocking as explained above.

Evidently, our propagator with the employed choice of free parameters (a) does not allow for an accurate description of the Coulomb repulsion at short distances. To understand this issue, we repeat the simulations with a different combination $a_0 = 0$ and $t_0 = 0.04$ (parameter set b), which has already proven to be superior to parameter set (a) for the radial density in the $2D$ harmonic trap. The results are shown in Fig. 4 for different numbers of propagators. The data with $P = 2$ are nearly equal to the results from parameters (a) and $P = 5$. The data for $P = 4$ and $P = 5$ almost coincide and are significantly increased with respect to the other curves. The main reason for the improved convergence of parameter set

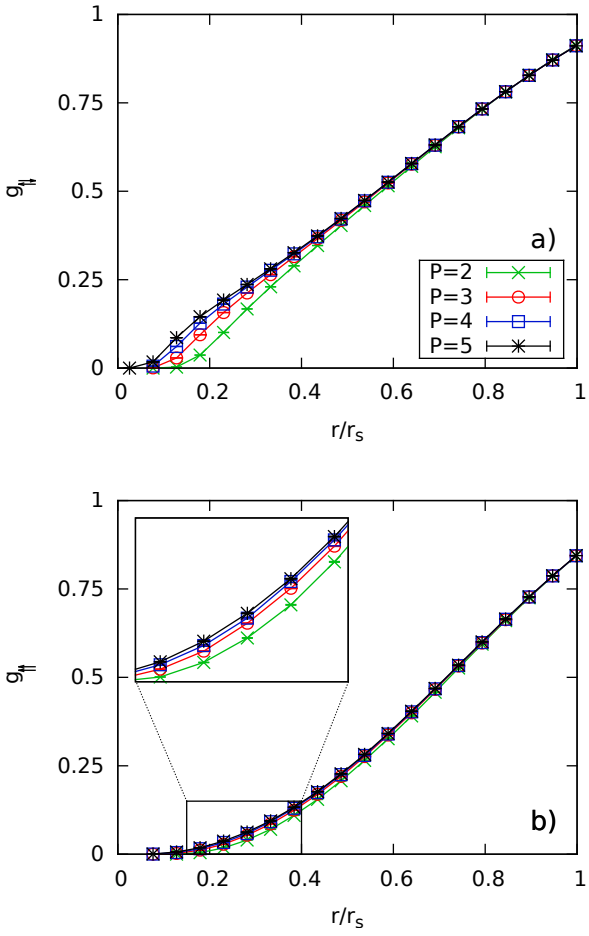

Figure 3: Convergence of the pair distribution function for $N = 4$ unpolarized electrons at $\theta = 1$ and $r_s = 4$ – Shown are PB-PIMC results for the inter- ($g_{\uparrow\downarrow}$, panel a) and intra-species ($g_{\uparrow\uparrow}$, panel b) distribution function for different numbers of propagators P and the fixed free parameters $a_1 = 0.33$ and $t_0 = 0.14$.

(b) is the choice $a_0 = 0$, which means that the forces are only taken into account on intermediate time slices. Due to the diagonality of the pair distribution function in coordinate space, it is measured exclusively on the main slices, for whose distribution the force terms do not directly enter. For this reason, the inter-species pair distribution function is not as drastically affected by the divergence of the $F(r) \propto 1/r^2$ terms at small r and the convergence of this quantity is significantly improved. For completeness, in panel b) we again show results for $g_{\uparrow\uparrow}$, which, for parameter set (b), are almost converged even for two propagators. It is important to note that while the description of the Coulomb repulsion at very short ranges is particularly challenging, this does not predominate in larger systems since the average number of particles within distance $r \in [\tilde{r}, \tilde{r} + \Delta\tilde{r})$ increases as $N(\tilde{r}) \propto \tilde{r}^2$. For $N = 66$ unpolarized electrons, which is the standard system size within this work, these effects are by far not

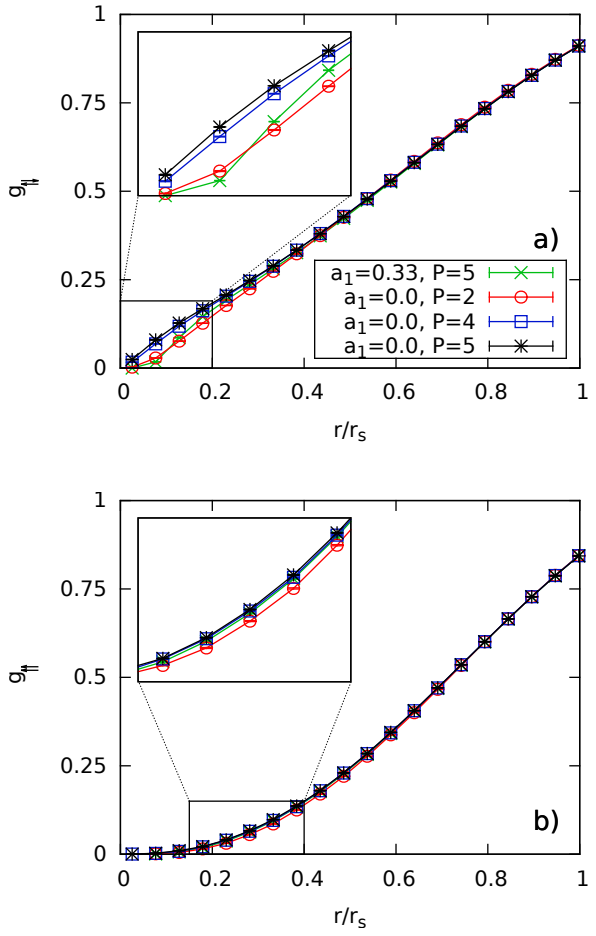

Figure 4: onvergence of the pair distribution function for $N = 4$ unpolarized electrons at $\theta = 1$ and $r_s = 4$ – Shown is the same information as in Fig. 3, but for a different combination of free parameters, i.e., $a_0 = 0$ and $t_0 = 0.04$.

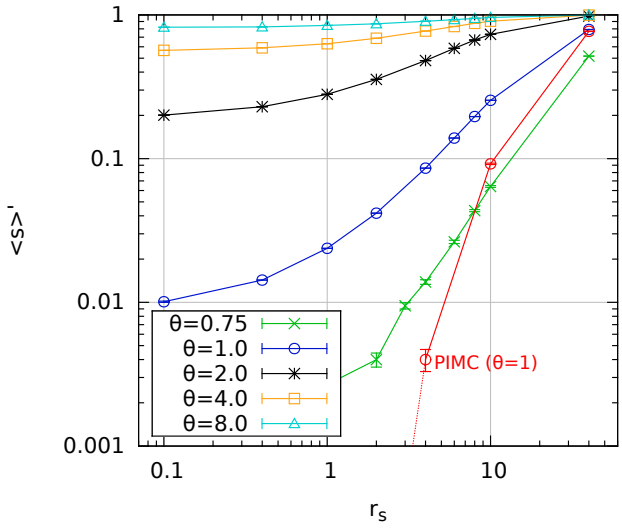

Figure 5: Average sign for PB-PIMC simulations of $N = 66$ unpolarized electrons at different temperatures – All PB-PIMC data have been obtained for $P = 2$ with $a_0 = 0.33$ and $t_0 = 0.14$ and the standard PIMC data (red curve) have been taken from Ref. [21].

as important and, for the same combination of r_s and θ as in Fig. 4, both the inter- and intra-species distribution function are of much higher quality, cf. Fig. 12.

Up to this point, only data for small benchmark systems with $N = 4$ electrons have been presented. To obtain meaningful results for the UEG, we simulate $N = 66$ unpolarized electrons, which is a commonly used model system since it corresponds to a closed momentum shell and, therefore, is well suited as a starting point for an extrapolation to the thermodynamic limit (finite size corrections). In Fig. 5, the average sign, cf. Eq. (20), is plotted versus the density parameter r_s for five different temperatures. For $\theta = 2, 4, 8$, $\langle s \rangle'$ is almost equal to unity for $r_s = 40$ and decreases just a trifle towards higher density, until it saturates at $r_s \sim 0.5$. Consequently, simulations are possible over the entire density range with relatively small computational effort. The slight increase of $\langle s \rangle'$ around $r_s \in [1, 10]$ is a nonideality effect: At high density, the system is approximately ideal and the Fermi temperature θ_F is an appropriate measure for quantum degeneracy. With increasing r_s, coupling effects become more important, which leads to a stronger separation of the electrons. Thus, there is less overlap of the kinetic density matrices and the determinants become exclusively positive. For $\theta = 1$, the average sign already significantly deviates from unity at $r_s = 40$ and exhibits a more severe decrease towards smaller r_s. Nevertheless, it attains a finite value $\langle s \rangle' \approx 0.01$ even at high density $r_s = 0.1$, which means that simulations are more involved but still manageable over the entire coupling range. This is in stark contrast to standard PIMC without the permutation blocking (red circles), for which the sign exhibits a sharp drop and simulations become unfeasible below $r_s \approx 5$. Finally, the green curve corresponds to $\theta = 0.75$ where PB-PIMC is capable to provide accurate results for $r_s \geq 3$.

B. Configuration PIMC

1. *Basic idea*

In this section, the main aspects of our CPIMC approach are explained. A detailed derivation of the CPIMC expansion of the partition function and the utilized Monte Carlo steps for the polarized UEG can be found in Refs. [22, 24].

For CPIMC, instead of evaluating the trace of the partition function Eq. (6) in coordinate representation, we switch to second quantization and perform the trace with anti-symmetrized $N-$particle states (Slater-

determinants)

$$|\{n\}\rangle = |n_1, n_2, \dots\rangle \,, \tag{16}$$

with n_i being the fermionic occupation number ($n_i \in \{0,1\}$) of the i-th spin-orbital $|\mathbf{k}_i\sigma_i\rangle$, where we choose the ordering of orbitals such that even (odd) orbital numbers have spin-up (spin-down) $\sigma = \uparrow$ ($\downarrow$). In this representation, fermionic anti-symmetry is automatically taken into account via the anti-commutation relations of the creation and annihilation operators, and thus, an explicit anti-symmetrization of the density operator is not needed. The expansion of the partition function is based on the concept of continuous time QMC, e.g., Refs. [45, 46], where the Hamiltonian is split into a diagonal and off-diagonal part $\hat{H} = \hat{D} + \hat{Y}$ with respect to the chosen basis. Summing up the entire perturbation series of the density operator $e^{-\beta\hat{H}}$ in terms of $\hat{Y}$ finally yields

$$Z = \sum_{\substack{K=0,\\ K\neq 1}}^{\infty} \sum_{\{n\}} \sum_{s_1 \dots s_{K-1}} \int_0^\beta d\tau_1 \int_{\tau_1}^\beta d\tau_2 \dots \int_{\tau_{K-1}}^\beta d\tau_K \tag{17}$$
$$(-1)^K e^{-\sum_{i=0}^{K} D_{\{n^{(i)}\}}(\tau_{i+1}-\tau_i)} \prod_{i=1}^{K} Y_{\{n^{(i)}\},\{n^{(i-1)}\}}(s_i) \,,$$

with the Fock space matrix elements of the diagonal and off-diagonal operator

$$D_{\{n^{(i)}\}} = \sum_l \mathbf{k}_l^2 n_l^{(i)} + \sum_{l<k} w^-_{lklk} n_l^{(i)} n_k^{(i)} \,, \tag{18}$$

$$Y_{\{n^{(i)}\},\{n^{(i-1)}\}}(s_i) = w^-_{s_i} (-1)^{\alpha_{s_i}} \,. \tag{19}$$

Here, $s_i = (pqrs)$ defines the four occupation numbers in which $\{n^{(i)}\}$ and $\{n^{(i-1)}\}$ differ, where it is $p < q$ and $r < s$. In this notation, the exponent of the fermionic phase factor is given by

$$\alpha_{s_i} = \alpha^{(i)}_{pqrs} = \sum_{l=p}^{q-1} n_l^{(i-1)} + \sum_{l=r}^{s-1} n_l^{(i)} \,.$$

Due to the trace, each summand in Eq. (17) fulfills $\{n\} = \{n^{(0)}\} = \{n^{(K)}\}$ and hence can be interpreted as a β-periodic path in Fock space. An example of such a path for the case of an unpolarized UEG is depicted in Fig. 6. The starting determinant $\{n\}$ at $\tau = 0$ undergoes K excitations of type s_i at time τ_i, which we refer to as "kinks". The weight of each path is computed according to the second line of Eq. (17), which can be both positive and negative. Since the Metropolis algorithm[43] can only be applied to strictly positive weights, we have to take the modulus of the weights in our MC procedure and compute expectation values according to

$$\langle O \rangle = \frac{\langle Os \rangle'}{\langle s \rangle'} \,, \tag{20}$$

where O is the corresponding Monte Carlo estimator of the observable, $\langle\cdot\rangle'$ denotes the expectation value with respect to the modulus weights, and s measures the sign of each path. Therefore, $\langle s \rangle'$ is the *average sign* of all sampled paths during the MC simulation. It is straightforward to show that the relative statistical error of observables computed according to Eq. (20) is inversely proportional to the average sign. As a consequence, in practice, reliable expectation values can be obtained if the average sign is larger than about 10^{-4}.

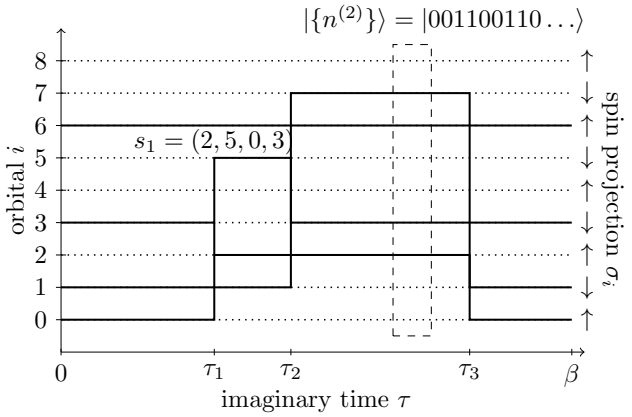

Figure 6: Typical closed path of $N = 4$ unpolarized particles in Slater determinant (Fock) space. The state with four occupied orbitals $|\mathbf{k}_0\uparrow\rangle, |\mathbf{k}_1\downarrow\rangle, |\mathbf{k}_3\downarrow\rangle, |\mathbf{k}_6\uparrow\rangle$ undergoes a two-particle excitation s_1 at time τ_1 replacing the occupied orbitals $|\mathbf{k}_0\uparrow\rangle, |\mathbf{k}_3\downarrow\rangle$ by $|\mathbf{k}_2\uparrow\rangle, |\mathbf{k}_5\downarrow\rangle$. Two further excitations occur at τ_2 and τ_3. The states at the "imaginary times" $\tau = 0$ and $\tau = \beta$ coincide. In addition, the total spin projection is conserved at any time. All possible paths contribute to the partition function Z, Eq. (17).

2. *Application to the unpolarized UEG*

The difference between CPIMC simulations of the polarized and unpolarized UEG enters basically in two ways. First, in addition to the particle number N, the total spin projection in the summation over the starting determinant $\{n^{(0)}\}$ in Eq. (17) has to be fixed, i.e., the number of spin-up $N_\uparrow$ and spin-down electrons $N_\downarrow$. Thus, if a whole occupied orbital is excited during the MC procedure (for details see Ref. [24]), it can only be excited to an orbital with the same spin projection. For example, orbital 6 in Fig. 6 could only be excited to orbital 8 or some higher unoccupied orbital with spin up (not pictured). Moreover, when adding a kink or changing two kinks via some two-particle excitation, it is most effective to include spin conservation in the choice of the four involved orbitals, since all other proposed excitations would be rejected due to a vanishing weight.

For the second aspect, we have to explicitly consider the modulus weight of some kink $s_i = (pqrs)$, which is

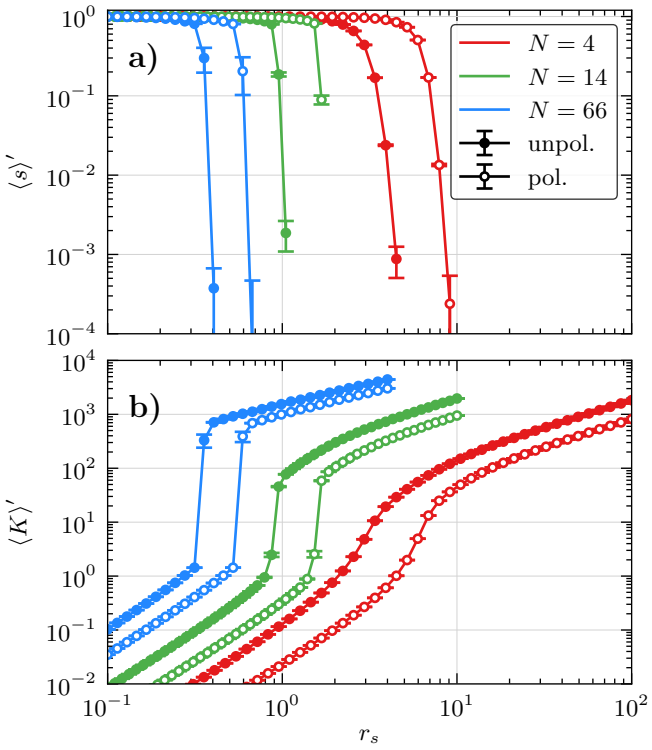

Figure 7: Average sign **a)** and average number of kinks **b)** of direct CPIMC, plotted versus the density parameter for three different particle numbers $N = 4, 14, 66$ in $N_B = 2109, 4169, 5575$ plane wave basis functions, respectively, at $\theta = 1$. Shown are the results from the simultation of the polarized (circles) and unpolarized (dots) UEG, where for the unpolarized case $2 \cdot N_B$ spin-orbitals have been used.

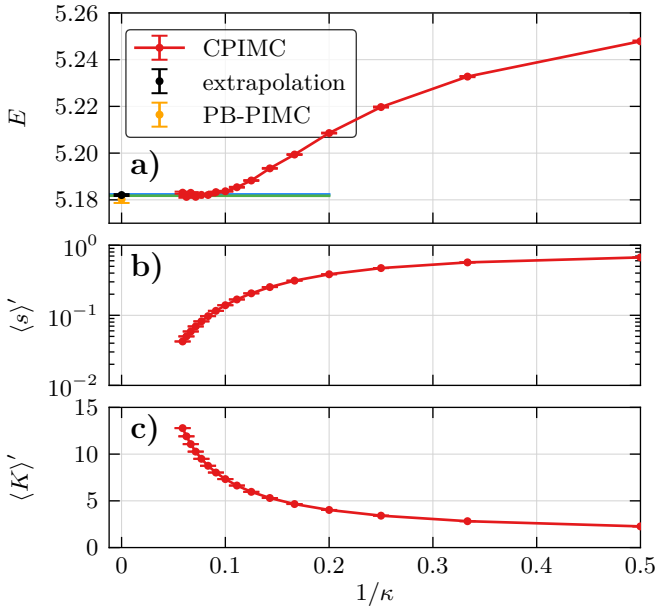

Figure 8: Convergence of **a)** the internal energy, **b)** the average sign and **c)** the average number of kinks with respect to the kink potential parameter κ of $N = 66$ unpolarized electrons at $r_s = 2$ and $\theta = 4$ in $N_B = 88946$ spin orbitals. The potenital parameter δ has been fixed to one. The blue (green) line show a horizontal (linear) fit to the last converged points. The asymptotic value (black point) in the limit $1/\kappa \to 0$ is enclosed between the blue and green lines and, within error bars, coincides with the PB-PIMC result (orange points).

given by the modulus of Eq. (19)

$$|Y_{\{n^{(i)}\},\{n^{(i-1)}\}}(s_i)| = \left| \frac{1}{(\mathbf{k}_p - \mathbf{k}_r)^2} \delta_{\sigma_p,\sigma_r} \delta_{\sigma_q,\sigma_s} - \frac{1}{(\mathbf{k}_p - \mathbf{k}_s)^2} \delta_{\sigma_p,\sigma_s} \delta_{\sigma_q,\sigma_r} \right| \cdot \frac{4\pi e^2}{L^3} \delta_{\mathbf{k}_p + \mathbf{k}_q, \mathbf{k}_r + \mathbf{k}_s} \,, \tag{21}$$

where we have used the definition of the anti-symmetrized two-electron integrals from Sec. II B. If all of the involved spin-orbitals have the same spin projection, the Kronecker deltas due to the spin obviously equal one, and the two-electron integrals are efficiently blocked, i.e., in most (momentum conserving) cases it is $|w^-_{pqrs}| < |w_{pqrs}|$ and $|w^-_{pqrs}| < |w_{pqsr}|$. However, if the involved orbitals have different spin projections, one of the two terms in Eq. (21) is always zero and $|w^-_{pqrs}| = |w_{pqsr}|$ or $|w^-_{pqrs}| = |w_{pqrs}|$. Hence, for otherwise fixed system parameters, the average weight of kinks in the unpolarized system is significantly larger. Since the diagonal matrix elements, cf. Eq. (18), are independent of the spin, there ought to be more kinks in simulations of the unpolarized system, which in turn results in a smaller sign, because each kink enters the partition function with three possible sign changes.

We address this issue in Fig. 7, where we plot the average sign **a)** and the average number of kinks **b)** for the polarized (circles) and unpolarized (dots) UEG of $N = 4, 14$ and 66 electrons at $\theta = 1$. Coming from small values of r_s, the average number of kinks grows linearly with r_s. Depending on the particle number, at some critical value of r_s, it starts growing exponentially, until it eventually turns again into a linear dependency. The onset of the exponential growth is connected to a drop of the average sign due to the combinatorial growth of potential sign changes in the sampled paths with increasing number of kinks. This behavior becomes more extreme the larger the particle number, both for the polarized and unpolarized system, so that for $N = 66$ electrons (blue lines), the average number of kinks suddenly increases from less than about two to a couple of hundred, which corresponds to a drop of the average sign from almost one to below 10^{-3}. However, for the unpolarized system, the critical value of r_s at which the average sign starts dropping drastically is approximately half of that of the polarized system containing the same number of electrons. In practice, this means that for $N = 66$ polarized electrons at $\theta = 1$ direct CPIMC calculations are feasible up to $r_s \sim 0.6$, whereas for $N = 66$ unpolarizd electrons direct CPIMC is applicable only up to $r_s \sim 0.3$.

3. Auxiliary kink potential

In Ref. [22], it has been shown that the use of an auxiliary kink potential of the form

$$V_{\delta,\kappa}(K) = \frac{1}{e^{-\delta(\kappa-K+0.5)}+1} \tag{22}$$

significantly extends the applicability range of our CPIMC method towards larger values of r_s. This is achieved by adding the potential to the second line of the partition function Eq. (17), i.e., multiplying the weight of each path with the potential. Obviously, since $V_{\delta,\kappa}(K) \to 1$ in the limit $\kappa \to \infty$, performing CPIMC simulations for increasing values of κ at fixed δ always converges to the exact result. Yet, to ensure a monotonic convergence of the energy, it turned out that the value of δ has to be sufficiently small. Both for the polarized and unpolarized system, choosing $\delta = 1$ is sufficient. In fact, the potential is nothing but a smooth penalty for paths with a larger number of kinks than κ.

In Fig. 8, we show the convergence of **a)** the internal energy (per particle), **b)** the average sign and **c)** the average number of kinks with respect to the kink potential parameter κ of $N = 66$ unpolarized electrons at $r_s = 2$ and $\theta = 4$. We have performed independent CPIMC simulations for different κ, using integer values from 2 to 17. While the energy almost remains constant for $\kappa \geq 10$ with a corresponding average sign larger than 0.1, the average sign and number of kinks themselves clearly are not converged. Further, the direct CPIMC algorithm (without the kink potential) would give a couple of thousand kinks with a practically vanishing sign. However, for the convergence of observables like the energy, apparently, a significantly smaller number of kinks is sufficient. This can be explained by a near cancellation of all additional contributions of the sampled paths with increasing number of kinks. For a detailed analysis, see Ref. [22].

We generally observe an s-shaped convergence of observables with $1/\kappa$, where the onset of the cancellation and near convergence are clearly indicated by the change in curvature. This allows for a robust extrapolation scheme to the asymptotic limit $1/\kappa \to \infty$, which is explained in detail in Ref. [22]. An upper (lower) bound of the asymptotic value is obtained by a horizontal (linear) fit to the last points after the onset of convergence. The extrapolated result is then computed as the mean value of the lower and upper bounds with the uncertainty estimated as their difference. In Fig. 8, both, the horizontal (blue line) and linear fit (green line) almost coincide due to the complete convergence (within statistical errors) of the last points. The asymptotic CPIMC result (black dot) perfectly agrees (within error bars) with the PB-PIMC result (orange dot). This confirms the validity of using the kink potential also for the unpolarized UEG.

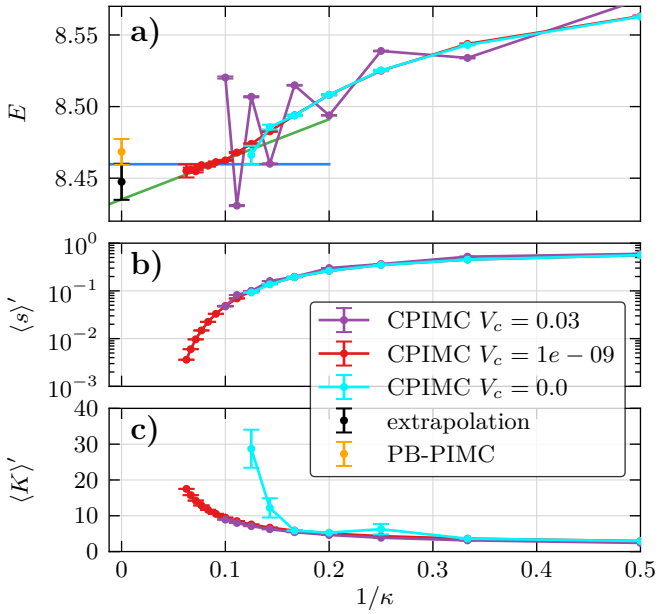

Figure 9: Convergence of **a)** the internal energy, **b)** the average sign and **c)** the average number of kinks with respect to the kink potential parameter κ of $N = 66$ unpolarized electrons at $r_s = 0.8$ and $\theta = 1$ in $N_B = 11150$ spin orbitals. The potential parameter δ has been fixed to one. The three curves correspond to CPIMC calculations where the kink potential has been cut off at different values V_c, i.e., $V_{1,\kappa}(K)$ (cf. Eq. (22)) is set to zero if it takes values smaller than V_c. The blue (green) line shows a horizontal (linear) fit to the last converged red points. The asymptotic value (black point) in the limit $1/\kappa \to 0$ is enclosed between the blue and green lines and, within error bars, coincides with the PB-PIMC result (orange points).

4. Further enhancement of the kink potential

It turns out that, in case of the unpolarized UEG, even with the use of a kink potential with $\delta = 1$, the simulation may approach paths with an extremely large number of kinks. This is demonstrated by the turquoise data points in Fig. 9 **c**), where the average number of kinks is shown for $N = 66$ unpolarized electrons at $\theta = 1$ and $r_s = 0.8$. For example, at $\kappa = 8$, there are on average about 30 kinks. However, increasing the penalty for paths with a number of kinks larger than κ, by increasing δ, is not a solution, since this would cause a non-monotonic convergence, oscillating with even and odd numbers of κ, as has been demonstrated in Ref. [22]. Therefore, we choose a different strategy which is justified by the fact that paths with a very large number of kinks do not contribute to physical observables, cf. Sec. III B 3 and Ref. [22]: we cut off the potential once it has dropped below some critical value V_c, thereby completely prohibiting paths where $V_{1,\kappa}(K) < V_c$. If the cut-off value is too large, we again recover an oscillating convergence behavior of the energy with even and odd numbers of κ rendering an extrapolation difficult. This is shown by the purple data points

in Fig. 9 **a)**, where the simulations have been performed with $V_c = 0.03$ so that paths with a number of kinks larger than $\kappa+3$ are prohibited. On the other hand, if we set $V_c = 10^{-9}$, so that paths with up to $\kappa + 20$ kinks are allowed, the oscillations vanish (within statistical errors) and we can again apply our extrapolation scheme. Indeed, even with the additional cut-off the extrapolated value (black dot) coincides with that of the PB-PIMC simulation (orange dot) within error bars. In all simulations presented below we have carefully verified that the cut-off value is sufficiently small to guarantee converged results.

To summarize, as for the polarized UEG [22], the accessible range of density parameters r_s of our CPIMC method can be extended by more than a factor two by the use of a suitable kink potential, in simulations of the unpolarized UEG as well. For example, at $\theta = 1$ direct CPIMC simulations are feasible up to $r_s \sim 0.3$, see Fig. 7, whereas the kink potential allows us to obtain accurate energies up to $r_s = 0.8$, as demonstrated in Fig. 9. In addition to the extrapolation scheme that has been introduced before for the spin-polarized case [22], we have cut off the potential at a sufficiently small value to prevent the simulation paths from approaching extremely large numbers of kinks. We expect this enhancement of CPIMC to be useful for arbitrary systems. In particular, it will allow us to further extend our previous results for the polarized UEG to larger r_s-values.

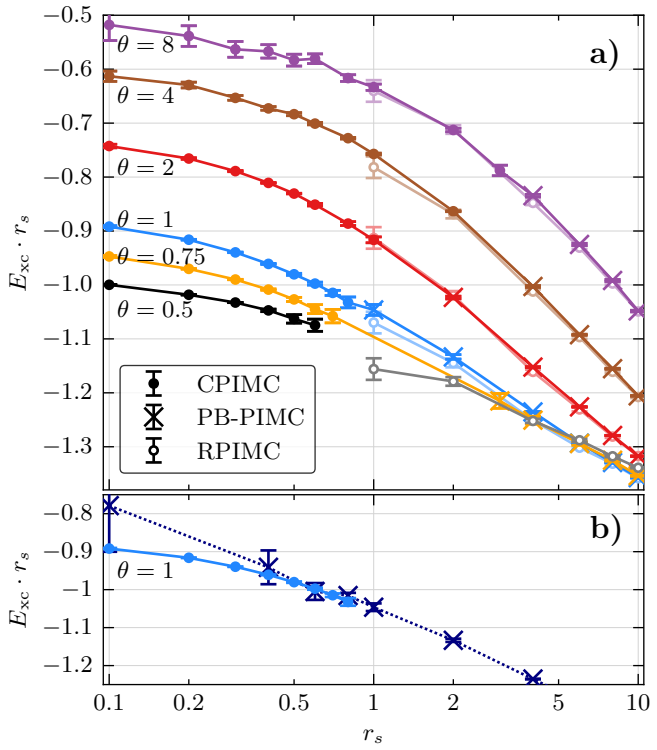

Figure 10: Exchange-correlation energy E_{xc} times r_s of the unpolarized $N = 66$ particle UEG over the density parameter r_s for different temperatures. In graphic **a)**, only the best results from CPIMC (dots) or PB-PIMC (crosses) calculations are shown, cf. table I in the appendix. In addition, RPIMC results by Brown *et al.*[21, 50] are plotted for comparison (lines with light colors and open circles). Graphic **b)** also shows PB-PIMC data for $r_s < 1$ at $\theta = 1$.

IV. COMBINED CPIMC AND PB-PIMC RESULTS

A. Exchange correlation energy

The exchange-correlation energy per particle, E_{xc}, of the uniform electrons gas is of central importance for the construction of density functionals and, therefore, has been the subject of numerous previous studies, e.g., Refs. [21, 22, 25, 47–49]. It is defined as the difference between the total energy of the correlated system and the ideal energy U_0,

$$E_{xc} = E - U_0 \; . \tag{23}$$

In Fig. 10 a), we show results for this quantity for six different temperatures in dependence on the density parameter r_s. All data are also available in Tab. I in the appendix. In order to fully exploit the complementary nature of our two approaches, we always present the most accurate data from either CPIMC (dots) or PB-PIMC (crosses). This allows us to cover the entire density range for $\theta \geq 1$, since here, the two methods allow for an overlap with respect to r_s. For completeness, we mention that the apparently larger statistical uncertainty for $\theta = 8$ in comparison to lower temperature is not a peculiar manifestation of the FSP, but, instead, an artifact due to the definition (23). At high temperature, the system becomes increasingly ideal and, therefore, the total energy E approaches U_0. To obtain E_{xc} at $\theta = 8$, a large part of E is subtracted, which, obviously, means that the comparatively small remainder is afflicted with a larger statistical uncertainty.

To illustrate the overlap between PB-PIMC and CPIMC, we show all available data points for $\theta = 1$ for both methods in panel b). This is the lowest temperature for which this is possible and, therefore, the most difficult example, because the systematic propagator error from PB-PIMC at small r_s is most significant here. Evidently, both data sets are in excellent agreement with each other and the deviations are well within the error bars. Although we do expect that the deterioration of the convergence of the PB-PIMC factorization scheme for small r_s, cf. Fig. 2, should become less severe for larger systems, any systematic trend is masked by the sign problem anyway and cannot clearly be resolved for the given statistical uncertainty.

Let us now consider temperatuers below $\theta = 1$. For $\theta = 0.75$, CPIMC is applicable only for $r_s \leq 0.7$, while PB-PIMC delivers accurate results for $r_s \geq 3$. Thus, the intermediate regime remains, without further improvements, out of reach and, for $\theta = 0.5$, PB-PIMC is not applicable for $N = 66$ unpolarized electrons in this density

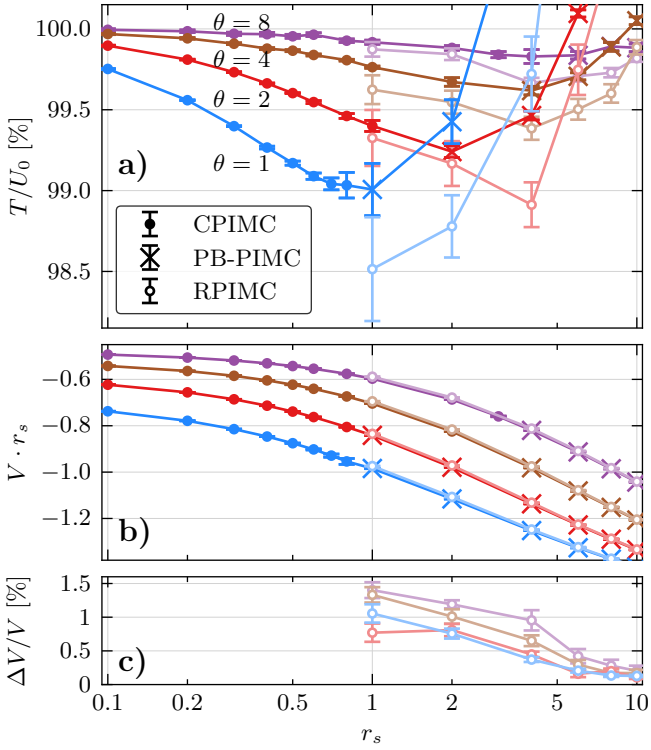

Figure 11: Kinetic (a) and potential (b) energy of the unpolarized $N = 66$ particle UEG over the density parameter r_s for different temperatures. Panel c) shows the relative difference between our results and RPIMC data by Brown *et al.* [21, 50].

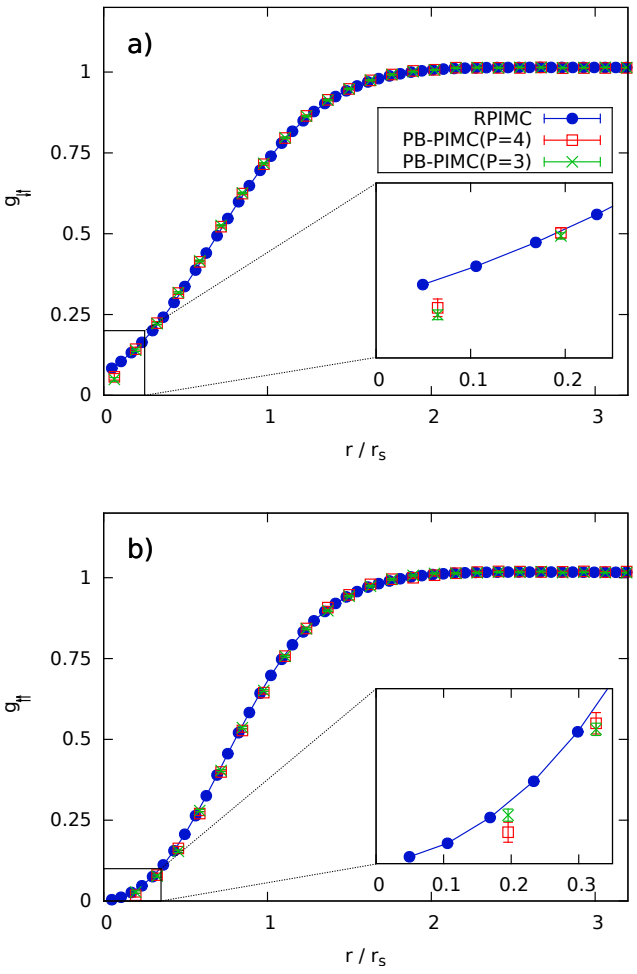

Figure 12: Pair distribution function of $N = 66$ unpolarized electrons at $r_s = 4$ and $\theta = 1$ – The PB-PIMC results have been obtained for $t_0 = 0.04$ and $a_1 = 0$, and the RPIMC data are taken from Ref. [21].

regime at all.

The comparison of our new combined results to the RPIMC data by Brown *et al.* [21], which are available for $r_s \geq 1$, reveals excellent agreement for the three highest temperatures, $\theta = 2, 4, 8$. For $\theta = 1$, all results are still within single error bars, but the RPIMC data appear to be systematically too low. This observation is confirmed for $\theta = 0.5$, where the fixed node approximation seems to induce an even more significant drop of E_{xc}. For completeness, we mention that although a similar trend has been found for the spin-polarized UEG as well [22, 25, 27], the overall agreement between RPIMC and our independent results is a little better for the unpolarized case.

Finally, we consider the kinetic and potential contribution, K and V, to the total energy separately. In Fig. 11 a), the kinetic energy in units of the ideal energy U_0 is plotted versus r_s and we again observe excellent agreement between PB-PIMC and CPIMC for all four shown temperatures. The RPIMC data, on the other hand, exhibit clear deviations and are systematically too low even for $r_s = 10$. In panel b), we show the same information for the potential energy, but the large V-range prevents us from resolving any differences between the different data sets. For this reason, in panel c), we explicitly show the relative differences between our new results and those from RPIMC. Evidently, the latter are systematically too high and the relative deviations increase with density exceeding $\Delta V/V = 1\%$. Curiously, $\Delta V/V$ attains its largest value for the highest temperature, $\theta = 8$, which contradicts the usual assumption that the nodal error decreases with increasing θ. Yet, in case of the exchange correlation energy, cf. Fig. 10, this trend seems to hold.

We summarize that, while RPIMC exhibits significant deviations for both K and V separately, these almost exactly cancel and, therefore, the total energy (and E_{xc}) is in rather good agreement with our results. This trend is in agreement with previous observations for the spin-polarized case [27].

B. Pair distribution function

Up to this point, we have compared RPIMC data for various energies (E_{xc}, V, K) to our independent results.

However, since only the total energy was in agreement while V and K both deviated, it remains an open question how other thermodynamic quantities are affected by the fixed node approximation. To address this issue, in Fig. 12 we show results for the pair distribution function (PDF) of the $N = 66$ unpolarized electrons at $r_s = 4$ and $\theta = 1$. This appears to be the most convenient parameter combination for a comparison since, on the one hand, there are significant differences for both K and V while, on the other hand, simulations with PB-PIMC are possible up to $P = 4$, which allows for accurate results of both $g_{\uparrow\uparrow}$ and $g_{\uparrow\downarrow}$. In panel a), the inter-species PDF $g_{\uparrow\downarrow}$ is plotted versus r and shown are PB-PIMC results for $P = 3$ (green crosses) and $P = 4$ (red squares) as well as RPIMC data (blue circles) from Ref. [21]. All three curves agree rather well and exhibit a distinct exchange correlation hole for $r \leq 1.5 r_s$ and a featureless approach to unity at larger distances. The inset shows the short range part of the PDF, which is the only segment where deviations are visible. The PB-PIMC results for $P = 3$ and $P = 4$ are within each others error bars and, for the smallest resolved r, slightly below the RPIMC data, altough this trend hardly exceeds twice the error bars as well. The results for the intra-species PDF $g_{\uparrow\uparrow}$ show a similar picture, although short range configurations of two particles are even more suppressed due to the Pauli blocking. Again, there appears a slight difference between PB-PIMC and RPIMC, which, however, cannot clearly be resolved within the given statistical uncertainty. Therefore, we conclude that our independent simulation data are in good agreement with the fixed node approximation for both pair distribution functions despite the observed deviations in K and V for these particular system parameters.

V. DISCUSSION

In summary, we have successfully extended the combination of PB-PIMC and CPIMC, presented in paper I, to the unpolarized UEG and, thereby, presented unbiased *ab initio* results at finite temperature. For PB-PIMC, we have observed an increased propagator error at high density, i.e., at $r_s < 1$, compared to the polarized UEG. This issue arises from the absence of the Pauli blocking between electrons of different spin-polarization, making the combination with the complementary CPIMC approach indispensable.

On the other hand, CPIMC suffers from a significantly more severe FSP due to the increased configuration weight of inter-species kinks. To overcome this problem, we have developed an additional enhancement of our extrapolation scheme. The introduction of a (very small) cut-off parameter V_c in the auxiliary kink potential prevents the number of kinks from diverging and, thereby, significantly extends the parameter range where accurate simulations are feasible. We have demonstrated that CPIMC and PB-PIMC reveal excellent agreement, where both are available, and, in their combination, allow for accurate results over the entire density range, for $\theta \geq 1$ and $N = 66$ electrons.

Overall, the existing RPIMC data for the exchange correlation energy are in better agreement with our *ab initio* results than for the spin-polarized UEG, but there seems to be a similar unphysical systematic drop around $r_s = 1$ at low temperatures. Interestingly, the separate kinetic and potential contributions to the energy substantially deviate from our results by more than one percent. Furthermore, for the first time, we have presented a comparison of the pair distribution functions $g_{\uparrow\uparrow}(r)$ and $g_{\uparrow\downarrow}(r)$, which are in good agreement with RPIMC .

It remains an important issue of future work to perform an extrapolation to the macroscopic limit, i.e., the development of finite-size corrections, e.g., [31–33]. To this end simulations with substantially larger particle numbers are required which should be possible with the presented enhancements. Furthermore, we expect that the presented combination of the complementary CPIMC and PB-PIMC approaches can be successfully applied to numerous other Fermi systems, such as two-component plasmas [51–53] and atoms embedded in jellium [54–56].

Acknowledgements

This work is supported by the Deutsche Forschungsgemeinschaft via project BO 1366-10 and via SFB TR-24 project A9 as well as grant shp00015 for CPU time at the Norddeutscher Verbund für Hoch- und Höchstleistungsrechnen (HLRN).

Appendix

As a supplement to Figs. 10 and 11, we have listed all combined simulation data from PB-PIMC and CPIMC in Tab. I.

Table I: Energies per particle for $N = 66$ unpolarized electrons: ideal energy, U_0, kinetic energy, T, potential energy, V and exchange-correlation energy E_{xc}. While the unmarked results correspond to standard CPIMC simulations (without the auxiliary kink potential), the "a" marks CPIMC results that have been obtained by the extrapolation as explained in Sec. III B 3 and Ref. [22]. For the latter values, the error includes systematic effects. All other errors correspond to a 1σ standard deviation. A "b" marks results from PB-PIMC calculations. For CPIMC results, the utilized number of basis functions N_B is given in the last column and has been fixed for the same temperature. The ideal energies have been computed using the same number of basis functions as for the interacting system. Energies in units of Ryd.

θ	r_s	U_0	E_{kin}	E_{pot}	E_{xc}	N_B
0.50	0.1	374.8592(12)	373.463(6)	−8.601 29(19)	−9.997(6)	11 150
0.50	0.2	93.714 81(30)	93.1294(25)	−4.506(4)	−5.0911(25)	11 150
0.50	0.3	41.651 02(13)	41.3226(28)^a	−3.1130(10)^a	−3.4421(9)^a	11 150
0.50	0.4	23.428 70(8)	23.2220(29)^a	−2.409(4)^a	−2.618(6)^a	11 150
0.50	0.5	14.994 37(5)	14.871(18)^a	−1.992(20)^a	−2.126(16)^a	11 150
0.50	0.6	10.412 756(34)	10.327(15)^a	−1.702(33)^a	−1.791(19)^a	11 150
0.75	0.1	495.690(4)	494.119(16)	−7.900 80(19)	−9.472(17)	11 150
0.75	0.2	123.9225(10)	123.2322(29)	−4.160 57(12)	−4.8508(31)	11 150
0.75	0.3	55.0767(5)	54.672(4)^a	−2.894 13(31)^a	−3.2999(14)^a	11 150
0.75	0.4	30.980 62(26)	30.712(4)^a	−2.2506(18)^a	−2.5215(30)^a	11 150
0.75	0.5	19.827 60(17)	19.637(4)^a	−1.858(5)^a	−2.054(8)^a	11 150
0.75	0.6	13.769 16(12)	13.632(10)^a	−1.601(17)^a	−1.741(14)^a	11 150
0.75	0.7	10.116 12(9)	10.018(18)^a	−1.400(23)^a	−1.511(18)^a	11 150
0.75	3.0	0.550 767(5)	0.556(5)^b	−0.4098(8)^b	−0.405(5)^b	
0.75	4.0	0.309 806 0(26)	0.3173(18)^b	−0.3201(4)^b	−0.3127(18)^b	
0.75	6.0	0.137 692 0(12)	0.1469(6)^b	−0.224 88(13)^b	−0.2157(5)^b	
0.75	8.0	0.077 452 0(7)	0.086 10(19)^b	−0.174 28(6)^b	−0.165 63(19)^b	
0.75	10.0	0.049 569 0(4)	0.056 87(9)^b	−0.142 666(28)^b	−0.135 36(9)^b	
1.00	0.1	623.230(6)	621.686(15)	−7.375 11(9)	−8.918(17)	11 150
1.00	0.2	155.8074(15)	155.1203(34)	−3.893 59(12)	−4.581(4)	11 150
1.00	0.3	69.2477(7)	68.8312(18)	−2.715 61(11)	−3.1322(19)	11 150
1.00	0.4	38.9518(4)	38.6661(33)^a	−2.1165(8)^a	−2.4025(25)^a	11 150
1.00	0.5	24.929 18(24)	24.7222(32)^a	−1.7508(17)^a	−1.961(4)^a	11 150
1.00	0.6	17.311 93(17)	17.1543(34)^a	−1.503(4)^a	−1.663(4)^a	11 150
1.00	0.7	12.718 97(12)	12.597(5)^a	−1.327(10)^a	−1.450(7)^a	11 150
1.00	0.8	9.737 96(9)	9.644(8)^a	−1.192(16)^a	−1.290(13)^a	11 150
1.00	1.0	6.232 30(6)	6.170(10)^b	−0.9844(10)^b	−1.046(10)^b	
1.00	2.0	1.558 074(15)	1.5491(21)^b	−0.557 77(28)^b	−0.5667(21)^b	
1.00	4.0	0.389 518(4)	0.393 70(21)^b	−0.313 04(5)^b	−0.308 86(21)^b	
1.00	6.0	0.173 119 0(17)	0.178 63(15)^b	−0.221 07(4)^b	−0.215 56(15)^b	
1.00	8.0	0.097 380 0(9)	0.103 13(6)^b	−0.171 900(18)^b	−0.166 15(6)^b	
1.00	10.0	0.062 323 0(6)	0.067 639(31)^b	−0.141 041(11)^b	−0.135 725(31)^b	
2.00	0.1	1155.227(11)	1154.031(32)	−6.229 59(19)	−7.425(33)	18 342
2.00	0.2	288.8066(28)	288.258(7)	−3.279 71(9)	−3.828(7)	18 342
2.00	0.3	128.3585(12)	128.0151(35)	−2.286 48(6)	−2.630(4)	18 342
2.00	0.4	72.2017(7)	71.9583(17)	−1.783 68(6)	−2.0270(18)	18 342
2.00	0.5	46.2091(4)	46.0256(11)	−1.477 71(6)	−1.6612(11)	18 342
2.00	0.6	32.089 63(31)	31.9444(29)^a	−1.270 90(35)^a	−1.419(4)^a	18 342
2.00	0.8	18.050 42(17)	17.9532(27)^a	−1.0069(11)^a	−1.108(4)^a	18 342
2.00	1.0	11.552 27(11)	11.483(4)^a	−0.8440(32)^a	−0.916(5)^a	18 342
2.00	2.0	2.888 066(28)	2.8661(11)^b	−0.489 60(21)^b	−0.5115(11)^b	
2.00	4.0	0.722 017(7)	0.718 15(19)^b	−0.284 21(6)^b	−0.288 07(20)^b	
2.00	6.0	0.320 896 0(31)	0.321 20(7)^b	−0.204 649(24)^b	−0.204 34(8)^b	
2.00	8.0	0.180 504 0(17)	0.181 83(4)^b	−0.161 212(15)^b	−0.159 89(4)^b	
2.00	10.0	0.115 523 0(11)	0.117 282(28)^b	−0.133 507(13)^b	−0.131 748(32)^b	

Table I: *(continued)*.

θ	r_s	U_0	T	V	$E_{\rm xc}$	N_B
4.00	0.1	2245.508(30)	2244.80(9)	−5.420 45(19)	−6.13(10)	88 946
4.00	0.2	561.377(8)	561.050(26)	−2.819 69(9)	−3.147(27)	88 946
4.00	0.3	249.5008(34)	249.272(14)	−1.948 87(8)	−2.177(15)	88 946
4.00	0.4	140.3442(19)	140.173(8)	−1.510 66(7)	−1.682(8)	88 946
4.00	0.5	89.8203(12)	89.699(6)	−1.245 91(7)	−1.367(6)	88 946
4.00	0.6	62.3752(8)	62.275(4)	−1.067 61(6)	−1.168(4)	88 946
4.00	0.8	35.0861(5)	35.0182(19)	−0.842 05(6)	−0.9099(19)	88 946
4.00	1.0	22.455 08(30)	22.4019(15)	−0.704 05(7)	−0.7572(16)	88 946
4.00	2.0	5.613 77(8)	5.5953(15)[a]	−0.412 30(33)[a]	−0.4317(4)[a]	88 946
4.00	4.0	1.403 442(19)	1.3981(4)[b]	−0.245 35(17)[b]	−0.2507(4)[b]	
4.00	6.0	0.623 752(8)	0.621 92(14)[b]	−0.180 22(7)[b]	−0.182 05(16)[b]	
4.00	8.0	0.350 861(5)	0.350 47(9)[b]	−0.144 02(4)[b]	−0.144 41(11)[b]	
4.00	10.0	0.224 551 0(30)	0.224 66(5)[b]	−0.120 675(31)[b]	−0.120 56(7)[b]	
8.00	0.1	4445.13(11)	4444.88(27)	−4.930 48(19)	−5.18(29)	147 050
8.00	0.2	1111.281(27)	1111.12(9)	−2.529 94(12)	−2.69(10)	147 050
8.00	0.3	493.903(12)	493.75(5)	−1.728 64(9)	−1.88(5)	147 050
8.00	0.4	277.820(7)	277.730(30)	−1.326 90(8)	−1.417(31)	147 050
8.00	0.5	177.805(4)	177.724(22)	−1.085 05(7)	−1.166(22)	147 050
8.00	0.6	123.4757(30)	123.431(15)	−0.923 38(6)	−0.968(15)	147 050
8.00	0.8	69.4551(17)	69.404(7)	−0.719 97(5)	−0.771(8)	147 050
8.00	1.0	44.4513(11)	44.415(6)	−0.596 79(5)	−0.633(6)	147 050
8.00	2.0	11.112 81(27)	11.0997(16)	−0.343 29(5)	−0.3564(16)	147 050
8.00	3.0	4.939 03(12)	4.9312(9)[a]	−0.2532(5)[a]	−0.2626(33)[a]	147 050
8.00	4.0	2.778 20(7)	2.7746(6)[b]	−0.205 02(29)[b]	−0.2086(6)[b]	
8.00	6.0	1.234 757(30)	1.232 74(28)[b]	−0.152 14(15)[b]	−0.1542(4)[b]	
8.00	8.0	0.694 551(17)	0.693 79(18)[b]	−0.123 21(10)[b]	−0.123 96(23)[b]	
8.00	10.0	0.444 513(11)	0.443 99(11)[b]	−0.104 30(7)[b]	−0.104 82(13)[b]	

[1] L.B. Fletcher *et al.*, Observations of Continuum Depression in Warm Dense Matter with X-Ray Thomson Scattering, *Phys. Rev. Lett.* **112**, 145004 (2014)

[2] D. Kraus *et al.*, Probing the Complex Ion Structure in Liquid Carbon at 100 GPa, *Phys. Rev. Lett.* **111**, 255501 (2013)

[3] S.P. Regan *et al.*, Inelastic X-Ray Scattering from Shocked Liquid Deuterium, *Phys. Rev. Lett.* **109**, 265003 (2012)

[4] J.D. Lindl *et al.*, The physics basis for ignition using indirect-drive targets on the National Ignition Facility, *Phys. Plasmas* **11**, 339 (2004)

[5] S.X. Hu, B. Militzer, V.N. Goncharov, and S. Skupsky, First-principles equation-of-state table of deuterium for inertial confinement fusion applications, *Phys. Rev. B* **84**, 224109 (2011)

[6] O.A. Hurricane *et al.*, Fuel gain exceeding unity in an inertially confined fusion implosion *Nature* **506**, 343-348 (2014)

[7] R. Nora *et al.*, Gigabar Spherical Shock Generation on the OMEGA Laser *Phys. Rev. Lett.* **114**, 045001 (2015)

[8] M.R. Gomez *et al.*, Experimental Demonstration of Fusion-Relevant Conditions in Magnetized Liner Inertial Fusion *Phys. Rev. Lett.* **113**, 155003 (2014)

[9] P.F. Schmit *et al.*, Understanding Fuel Magnetization and Mix Using Secondary Nuclear Reactions in Magneto-Inertial Fusion *Phys. Rev. Lett.* **113**, 155004 (2014)

[10] R. Ernstorfer *et al.*, The Formation of Warm Dense Matter: Experimental Evidence for Electronic Bond Hardening in Gold, *Science* **323**, 5917 (2009)

[11] M.D. Knudson *et al.*, Probing the Interiors of the Ice Giants: Shock Compression of Water to 700 GPa and 3.8$\mathbf{g}/cm^3$, *Phys. Rev. Lett.* **108**, 091102 (2012)

[12] B. Militzer *et al.*, A Massive Core in Jupiter Predicted from First-Principles Simulations, *Astrophys. J.* **688**, L45 (2008)

[13] N. Nettelmann, A. Becker, B. Holst and R. Redmer, Jupiter Models with Improved Ab Initio Hydrogen Equation of State (H-REOS.2), *Astrophys. J.* **750**, 52 (2012)

[14] E.Y. Loh, J.E. Gubernatis, R.T. Scalettar, S.R. White, D.J. Scalapino and R.L. Sugar, Sign problem in the numerical simulation of many-electron systems, *Phys. Rev. B* **41**, 9301-9307 (1990)

[15] M. Troyer and U.J. Wiese, Computational Complexity and Fundamental Limitations to Fermionic Quantum Monte Carlo Simulations, *Phys. Rev. Lett.* **94**, 170201 (2005)

[16] D.M. Ceperley, Fermion Nodes, *J. Stat. Phys.* **63**, 1237-1267 (1991)

[17] B. Militzer and E.L. Pollock, Variational density matrix method for warm, condensed matter: Application to dense

hydrogen, *Phys. Rev. E* **61**, 3470-3482 (2000)
[18] B. Militzer, Ph.D. dissertation, University of Illinois at Urbana-Champaign (2000)
[19] V.S. Filinov, Cluster expansion for ideal Fermi systems in the 'fixed-node approximation', *J. Phys. A: Math. Gen.* **34**, 1665-1677 (2001)
[20] V.S. Filinov, Analytical contradictions of the fixed-node density matrix, *High Temp.* **52**, 615-620 (2014)
[21] E.W. Brown, B.K. Clark, J.L. DuBois and D.M. Ceperley, Path-Integral Monte Carlo Simulation of the Warm Dense Homogeneous Electron Gas, *Phys. Rev. Lett.* **110**, 146405 (2013)
[22] S. Groth, T. Schoof, T. Dornheim, and M. Bonitz, Ab Initio Quantum Monte Carlo Simulations of the Uniform Electron Gas without Fixed Nodes, arXiv: 1511.03598 (2015)
[23] T. Schoof, M. Bonitz, A.V. Filinov, D. Hochstuhl and J.W. Dufty, Configuration Path Integral Monte Carlo, *Contrib. Plasma Phys.* **51**, 687-697 (2011)
[24] T. Schoof, S. Groth and M. Bonitz, Towards ab Initio Thermodynamics of the Electron Gas at Strong Degeneracy, *Contrib. Plasma Phys.* **55**, 136-143 (2015)
[25] T. Schoof, S. Groth, J. Vorberger and M. Bonitz, *Ab Initio* Thermodynamic Results for the Degenerate Electron Gas at Finite Temperature, *Phys. Rev. Lett.* **115**, 130402 (2015)
[26] T. Dornheim, S. Groth, A. Filinov and M. Bonitz, Permutation blocking path integral Monte Carlo: a highly efficient approach to the simulation of strongly degenerate non-ideal fermions, *New J. Phys.* **17**, 073017 (2015)
[27] T. Dornheim, T. Schoof, S. Groth, A. Filinov, and M. Bonitz, Permutation Blocking Path Integral Monte Carlo Approach to the Uniform Electron Gas at Finite Temperature, *J. Chem. Phys.* **143**, 204101 (2015)
[28] V.M. Zamalin, G.E. Norman, and V.S. Filinov, The Monte-Carlo Method in Statistical Thermodynamics, Nauka, Moscow (1977)
[29] D.M. Ceperley, Path integrals in the theory of condensed helium, *Rev. Mod. Phys.* **67**, 279-355 (1995)
[30] D.M. Ceperley and B.J. Alder, Ground State of the Electron Gas by a Stochastic Method, *Phys. Rev. Lett.* **45**, 566 (1980)
[31] L.M. Fraser *et al.*, Finite-size effects and Coulomb interactions in quantum Monte Carlo calculations for homogeneous systems with periodic boundary conditions, *Phys. Rev. B* **53**, 1814 (1996)
[32] N.D. Drummond, R.J. Needs, A. Sorouri and W.M.C. Foulkes, Finite-size errors in continuum quantum Monte Carlo calculations, *Phys. Rev. B* **78**, 125106 (2008)
[33] C. Lin, F.H. Zong and D.M. Ceperley, Twist-averaged boundary conditions in continuum quantum Monte Carlo algorithms, *Phys. Rev. E* **64**, 016702 (2001)
[34] N.S. Blunt, T.W. Rogers, J.S. Spencer and W.M. Foulkes, Density-matrix quantum Monte Carlo method, *Phys. Rev. B* **89**, 245124 (2014)
[35] F.D. Malone *et al.*, Interaction Picture Density Matrix Quantum Monte Carlo, *J. Chem. Phys.* **143**, 044116 (2015)
[36] M. Takahashi and M. Imada, Monte Carlo Calculation of Quantum Systems, *J. Phys. Soc. Jpn.* **53**, 963-974 (1984)
[37] V.S. Filinov *et al.*, Thermodynamic Properties and Plasma Phase Transition in dense Hydrogen, *Contrib. Plasma Phys.* **44**, 388-394 (2004)
[38] A.P. Lyubartsev, Simulation of excited states and the sign problem in the path integral Monte Carlo method, *J. Phys. A: Math. Gen.* **38**, 66596674 (2005)
[39] M. Takahashi and M. Imada, Monte Carlo of Quantum Systems. II. Higher Order Correction, *J. Phys. Soc. Jpn.* **53**, 3765-3769 (1984)
[40] S.A. Chin and C.R. Chen, Gradient symplectic algorithms for solving the Schrödinger equation with time-dependent potentials, *J. Chem. Phys.* **117**, 1409 (2002)
[41] K. Sakkos, J. Casulleras and J. Boronat, High order Chin actions in path integral Monte Carlo, *J. Chem. Phys.* **130**, 204109 (2009)
[42] S.A. Chin, High-order Path Integral Monte Carlo methods for solving quantum dot problems, *Phys. Rev. E* **91**, 031301(R) (2015)
[43] N. Metropolis, A.W. Rosenbluth, M.N. Rosenbluth, A.H. Teller and E. Teller, Equation of State Calculations by Fast Computing Machines, *J. Chem. Phys.* **21**, 1087 (1953)
[44] P. Gori-Giorgi, F. Sacchetti, and G.B. Bachelet, Analytic Static Structure Factors and Pair-Correlation Functions for the Unpolarized Homogeneous Electron Gas, *Phys. Rev. B* **61**, 7353 (2000)
[45] N.V. Prokofev, B.V. Svistunov, and I.S. Tupitsyn, *Exact quantum Monte Carlo process for the statistics of discrete systems*, JETP Lett. **64**, 911 (1996) [Pisma Zh. Exp. Teor. Fiz. **64**, 853 (1996)].
[46] N.V. Prokofev, B.V. Svistunov, and I.S. Tupitsyn, *Exact, complete, and universal continuous-time worldline Monte Carlo approach to the statistics of discrete quantum systems*, JETP **87**, 310 (1998).
[47] E.W. Brown, J.L. DuBois, M. Holzmann and D.M. Ceperley, Exchange-correlation energy for the three-dimensional homogeneous electron gas at arbitrary temperature, *Phys. Rev. B.* **88**, 081102(R) (2013)
[48] V.V. Karasiev, T. Sjostrom, J. Dufty and S.B. Trickey, Accurate Homogeneous Electron Gas Exchange-Correlation Free Energy for Local Spin-Density Calculations, *Phys. Rev. Lett.* **112**, 076403 (2014)
[49] V.S. Filinov, V.E. Fortov, M. Bonitz and Zh. Moldabekov, Fermionic path integral Monte Carlo results for the uniform electron gas at finite temperature, *Phys. Rev. E* **91**, 033108 (2015)
[50] We take the energy values from the supplement of Ref. [21] and substract the finite size corrections. This allows for a meaningful comparison with the same model system of $N = 66$ unpolarized electrons.
[51] M. Bonitz, V.S. Filinov, V.E. Fortov, P.R. Levashov and H. Fehske, Crystallization in Two-Component Coulomb Systems, *Phys. Rev. Lett.* **95**, 235006 (2005)
[52] M.A. Morales, C. Pierleoni and D. Ceperley, Equation of state of metallic hydrogen from coupled electron-ion Monte Carlo simulations, *Phys. Rev. E* **81**, 021202 (2010)
[53] V.S. Filinov, M. Bonitz, H. Fehske, V.E. Fortov and P.R. Levashov, Proton Crystallization in a Dense Hydrogen Plasma, *Contrib. Plasma Phys.* **52**, 224-228 (2012)
[54] M.J. Puska, R.M. Nieminen, and M. Manninen, Atoms Embedded in an Electron Gas: Immersion Energies, *Phys. Rev. B* **24**, 3037 (1981)
[55] V.U. Nazarov, C.S. Kim, and Y. Takada, Spin Polarization of Light Atoms in Jellium: Detailed Electronic Structures, *Phys. Rev. B* **72**, 233205 (2005)
[56] M. Bonitz, E. Pehlke, and T. Schoof, Attractive Forces between Ions in Quantum Plasmas: Failure of Linearized

Quantum Hydrodynamics, *Phys. Rev. E* **87**, 033105 (2013)